

# The Luminosity of Population III Star Clusters

Alexander L. DeSouza and Shantanu Basu\*

*Department of Physics and Astronomy, The University of Western Ontario, 1151 Richmond Street, London, ON, Canada, N6A 3K7*

9 March 2015

## ABSTRACT

We analyze the time evolution of the luminosity of a cluster of Population III protostars formed in the early universe. We argue from the Jeans criterion that primordial gas can collapse to form a cluster of first stars that evolve relatively independently of one another (i.e., with negligible gravitational interaction). We model the collapse of individual protostellar clumps using 2+1D nonaxisymmetric numerical hydrodynamics simulations. Each collapse produces a protostar surrounded by a massive disk (i.e.,  $M_{\text{disk}}/M_* \gtrsim 0.1$ ), whose evolution we follow for a further 30–40 kyr. Gravitational instabilities result in the fragmentation and the formation of gravitationally bound clumps within the disk. The accretion of these fragments by the host protostar produces accretion and luminosity bursts on the order of  $10^6 L_{\odot}$ . Within the cluster, we show that a simultaneity of such events across several protostellar cluster members can elevate the cluster luminosity to  $5\text{--}10\times$  greater than expected, and that the cluster spends  $\sim 15\%$  of its star-forming history at these levels. This enhanced luminosity effect is particularly enabled in clusters of modest size with  $\simeq 10\text{--}20$  members. In one such instance, we identify a confluence of burst events that raise the luminosity to nearly  $1000\times$  greater than the cluster mean luminosity, resulting in  $L > 10^8 L_{\odot}$ . This phenomenon arises solely through the gravitational-instability-driven episodic fragmentation and accretion that characterizes this early stage of protostellar evolution.

**Key words:** accretion disks—cosmology: theory—hydrodynamics—stars: clusters—stars: formation—stars: Population III

## 1 INTRODUCTION

Following the emission of the Cosmic Microwave Background, the universe entered a cosmological “dark age” that ended with the formation of the first stars in the universe. These first stars (known as Population III stars) were responsible for producing the ultraviolet radiation that began the reionization of the universe (e.g., Tumlinson & Shull 2000), and their supernovae were responsible for enriching the intergalactic medium with the first heavy elements (e.g., Miralda-Escudé & Rees 1997; Gnedin & Ostriker 1997; Ferrara et al. 2000).

Cosmological-scale simulations that follow both the dark matter and baryonic components of the early universe have yielded the consensus opinion that Population III stars formed in dark matter minihalos with masses of approximately  $10^6 M_{\odot}$ . These  $3\sigma+$  perturbations over the background dark matter density field virialized by redshifts of  $z \sim 20\text{--}50$  (Tegmark et al. 1997; Abel et al. 2002; Bromm et al. 2002). With few exceptions (e.g., Turk et al. 2009), these simulations suggest that the gas pooling into the halos underwent a quasi-hydrostatic contraction until they had sufficient mass to trigger runaway gravitational collapse (Abel et al. 2002; Bromm et al. 2002; Bromm & Loeb 2004; Yoshida et al. 2006; O’Shea & Norman 2007; Yoshida et al. 2008). These studies estab-

lished the standard paradigm that the progenitor cloud cores of the first stars were most likely to have been massive and formed in relative isolation.

In contrast, it is well understood (theoretically as well as observationally) that most star formation in the present-day universe arises from the fragmentation of molecular clouds, resulting in a multiplicity of young stellar objects being formed in close proximity to each other (e.g., Carpenter et al. 1997; Hillenbrand 1997; Lada & Lada 2003). Motivated by this, several recent studies have explored the fragmentary nature of primordial gas in the early universe, and have been able to resolve fragmentation in the disk-like environments surrounding the first protostars, thus challenging the standard paradigm (Stacy et al. 2010; Clark et al. 2011; Greif et al. 2011; Vorobyov et al. 2013, hereafter VDB 2013).

Clearly some ambiguity remains regarding the initial conditions and the formation mechanism(s) of the first stars. Observations will be required to accurately distinguish between the many existing theories of Population III star formation and evolution. In fact, the detection of primordial star clusters and galaxies in the early universe has already been defined as a major goal for next generation telescopes (e.g., Windhorst et al. 2006). Bromm et al. (2001) were among the first to investigate the spectral energy distribution of primordial stars theoretically. Later studies have expanded on their results to show that isolated Population III stars are likely to be too faint for detection by instruments such as the forth-

\* e-mail: alexander.desouza@gmail.com, basu@uwo.ca

coming James Webb Space Telescope, even when their fluxes are enhanced via chance gravitational lensing (Rydberg et al. 2013). Several authors have also turned their attention toward the potential of observing clusters, dwarf galaxies, and massive galaxies that contain Population III stars that may have formed at lower redshifts (i.e.,  $z < 10$ ) due to inhomogeneous metal enrichment of the intergalactic medium following the first supernovae (e.g., Ciardi & Ferrara 2001; Scannapieco et al. 2003; Tornatore et al. 2007; Johnson 2010; Safranek-Shrader et al. 2014).

In this paper we propose a scenario for the formation of a cluster of Population III stars. We argue that the gas pooling into the dark matter halos in which the first stars formed is subject to the Jeans criterion analogously to the fragmentation of giant molecular clouds in the present-day universe. As a result, these halos were capable of producing small clusters of first stars. Using non-axisymmetric numerical hydrodynamics simulations, we study the gravitational-instability-driven fragmentation and accretion in the collapsing protostellar environment. The resulting burst mode of accretion is even more prominent in a Population III environment than in present-day star formation, as shown by VDB 2013. We use the calculations for individual cluster members to compile the frequency, magnitude, and luminosity of burst events for each cluster as a whole. We find that a simultaneity of accretion events can produce bursts of luminosity that are several orders of magnitude greater than the mean cluster luminosity.

The structure of this paper is as follows. In Section 2 we describe how gas that settles into the host dark matter halos is subject to the Jeans fragmentation criterion, allowing for the formation of a cluster of first stars. In Section 3 we describe our numerical simulations (as well as our selections for the initial conditions) for the formation of each protostar, and calculate the luminosity for each of these cluster members. In Section 4 we discuss the implications of having a multiplicity of protostars simultaneously experiencing bursts of accretion, and calculate the effect this has on the luminosity of the cluster. We also discuss the implications of this phenomenon for future observational programs. Finally, in Section 5 we conclude with a brief discussion of our results.

## 2 THE CASE FOR POPULATION III STAR CLUSTERS

The formation of a cluster of Population III stars is thought to begin with the collapse of low density baryon gas into the gravitational potential wells established by dark matter minihalos that have collapsed and virialized by  $z \sim 20$ –50. The gas to dark matter fraction in these halos is roughly 10%, and amounts to a gas mass of  $10^4$  to  $10^5 M_\odot$ . Numerical simulations of this collapse reveal that the gas streaming into these potential wells exhibits filamentary and knotty structure (e.g., Bromm et al. 1999; Clark et al. 2008; Greif et al. 2011). Indeed, gravity is well known to enhance such anisotropic structure during collapse (e.g., Lin et al. 1965).

The formation of  $H_2$  cools the gas efficiently (and lowering the Jeans mass) from temperatures of a few times 1000 K to a few times 100 K, allowing the gas density to increase to  $n \sim 10^4 \text{ cm}^{-3}$ . While the imprint of substructure exists within the gas morphology, the formation of  $H_2$  is inefficient for cooling the gas below a temperature of a few times 100 K, inhibiting further collapse. Instead, these precursor imprints of fragmentation must next undergo a slow quasi-hydrostatic contraction as they accrete additional mass (e.g., Tegmark et al. 1997; Abel et al. 2002; Bromm et al. 2002). Run-away gravitational collapse is only then triggered when the mass of these “weak clumps” exceeds the local Jeans value at this scale,

being (e.g., Clarke & Bromm 2003)

$$M_J \simeq 400 M_\odot \left( \frac{T}{300 \text{ K}} \right)^{3/2} \left( \frac{n}{10^5 \text{ cm}^{-3}} \right)^{-1/2}. \quad (1)$$

For example, a halo with a gas mass of  $10^5 M_\odot$  and a 10% star formation efficiency would form a weak cluster with  $\simeq 20$  members. Though this sequence of events differs slightly from that of present-day star formation, the latter also envisions a multiplicity of approximately Jeans mass fragments that form in close proximity to produce a weak or strong cluster (e.g., in Taurus and  $\rho$  Ophiuchus; Onishi et al. 1998; Johnstone et al. 2000).

These resultant massive clumps, each containing roughly  $400 M_\odot$  of gas, are the sites of first star formation within the halo. The dynamical state of a typical clump formed in this way—its mass, physical extent, temperature, and angular momentum—are all determined by the collapse process. The initial conditions for the further contraction of these clumps are therefore relatively well constrained (e.g., Yoshida et al. 2003, 2006).

Authors such as Abel et al. (1998) have estimated that the efficiency of this fragmentation—with which the gas pooling into the dark matter halo is assimilated into high-density clumps—could vary between as little as a few percent to nearly 50%. As the larger clumps tend to retain their individuality against dispersal and/or mergers, the final evolutionary state of the halo gas is expected to be a small cluster of isolated objects (e.g., Clark et al. 2008; Turk et al. 2009; Greif et al. 2012). However, owing to lingering ambiguities about the manner in which this occurs, we adopt the definition of a “cluster” as being any association of 2+ stars forming from independent gaseous clumps that result from the subfragmentation of primordially pristine gas that has pooled into a single dark matter halo. Additionally, we concern ourselves with only the formation period during which the cluster members have masses below  $40 M_\odot$ . This allows us to assume that the predominant gas fraction within the halo is not ionized by the star formation as the cluster evolution proceeds. In fact, such conditions represent the analogue of present-day so-called “embedded” clusters, in which more than 80% of the cluster members belong to the Class II/III evolutionary phases, and the mass function of the cluster is assumed to be no longer evolving (e.g., Gutermuth et al. 2009). We also assume that each clump is able to promptly form stars within  $\sim 1$  Myr, or roughly the lifetime of the most massive individual stars (e.g., Bond et al. 1984).

Some caveats to our model assumptions are that we are assuming cluster formation according to the standard hydrodynamic Jeans criterion, and disk evolution in the hydrodynamic limit. Cluster formation may be strongly affected by several other factors. Turbulence generated by colliding flows may leave a strong initial imprint that dominates fragmentation (Heitsch et al. 2006, 2008). Radiative feedback from the very first massive stars can also affect the further fragmentation of a cloud or disk (Stacy et al. 2012). Furthermore, if a seed magnetic field exists and is amplified by dynamo action during primordial cloud collapse (Turk et al. 2012), then magnetic field effects can significantly affect the Jeans scale (Ciolek & Basu 2006; Basu et al. 2009) and affect global mass flow in the cloud (Price & Bate 2008). Magnetic fields can also inhibit the formation of large disks or their fragmentation in simulations of present-day star formation (e.g., Mellon & Li 2008; Commerçon et al. 2010; Machida et al. 2011; Dapp et al. 2012; Tomida et al. 2015), and their effect in the Population III regime remains to be further elucidated.

### 3 INDIVIDUAL CLUSTER MEMBERS

The clumps that emerge from the fragmentation are assumed to be relatively isolated. Competition for accretion between clumps (due to protostellar crowding) and effects arising from gravitational interactions are negligibly small (e.g., Turk et al. 2009; Hirano et al. 2014). We thus model the formation and evolution of each cluster member with its own unique simulation—the initial conditions of which stem from the arguments of the preceding section. Here we provide details about the numerical aspects of our code, our specific choices of initial conditions, and investigate the long-term behavior exhibited in a fiducially constructed model.

#### 3.1 Numerical Simulations

We carry out numerical simulations of the gravitationally induced collapse of the primordial gas in 2+1D, assuming a thin-disk geometry. Our code is a modified version of that presented in Vorobyov & Basu (2005, 2006). The hydrodynamic equations are solved using a finite difference scheme with a time-explicit operator-split solution, based on Stone & Norman (1992). A thorough description of our code is presented in VDB 2013.

The mass and momentum transport equations in the thin disk limit can be expressed as

$$\frac{\partial \Sigma}{\partial t} + \nabla \cdot (\Sigma \mathbf{v}) = 0, \quad (2)$$

$$\frac{\partial}{\partial t} (\Sigma \mathbf{v}) + \nabla \cdot (\Sigma \mathbf{v} \otimes \mathbf{v}) = -\nabla P + \Sigma \mathbf{g}, \quad (3)$$

in which  $\Sigma$  is the surface mass density,  $\mathbf{v}$  is the velocity of the disk material,  $P$  is the vertically integrated pressure (determined assuming the disk is in vertical hydrostatic equilibrium at all times), and  $\nabla$  is the planar gradient operator. The gravitational acceleration in the plane of the disk ( $\mathbf{g}$ ) includes the contribution from the protostar (once formed), from material inside the sink cell, and from the self-gravity of the disk and surrounding cloud core. All vectorial terms and quantities are understood as having only  $\hat{r}$  and  $\hat{\phi}$  components in this formulation.

In order that the environment of the collapsing core accurately reflect primordial conditions, equations (2) and (3) are closed with a barotropic relation that fits the 1D core collapse simulations of Omukai et al. (2005). These include the detailed chemical and thermal processes of the collapsing gas. Additional details of our model are provided in VDB 2013.

#### 3.2 Initial Conditions

The initial conditions for the radial gas surface density  $\Sigma$  and angular velocity  $\Omega$  profiles for primordial cores are taken to be very similar to those of present-day star forming cores (e.g., Omukai & Nishi 1998; Vorobyov & Basu 2006; Yoshida et al. 2008; Vorobyov & Basu 2010),

$$\Sigma = \Sigma_0 \left( 1 + \left( \frac{r}{r_0} \right)^2 \right)^{-1/2}, \quad (4)$$

$$\Omega = 2\Omega_0 \left( \frac{r_0}{r} \right)^2 \left( \sqrt{1 + \left( \frac{r}{r_0} \right)^2} - 1 \right). \quad (5)$$

The radial surface mass density profile  $\Sigma$  is that of an integrated Bonnor-Ebert sphere (Dapp & Basu 2009), while the form of the

initial angular velocity profile  $\Omega$  corresponds to the differential rotation profile expected for a core collapsing out of a near-uniform initial surface density field (Basu 1997).

We constrain  $\Sigma_0$  by assuming a constant ratio of the radius of the outer computational boundary  $r_{\text{out}}$  to that of the centrally plateaued region  $r_0$ :  $r_{\text{out}}/r_0 \equiv 6$ ; so that each core has a similar initial form with  $\Sigma_0 \approx 0.25 \text{ g cm}^{-2}$ . The parameter  $r_{\text{out}}$  thus also determines the mass of the core, which for  $r_{\text{out}} = 0.5 \text{ pc}$  is approximately  $300 M_\odot$ . These choices are constant for each of the cores simulated, and is consistent with the typical size and mass found from ab initio cosmological simulations of the collapse of primordial starless cores (e.g., Yoshida et al. 2006).

The angular momentum of the cloud core is parameterized by  $\Omega_0$ —as appears in equation (5)—and is related to the dimensionless parameter  $\eta = (\Omega_0 r_0 / c_s)^2$  (Basu 1997).  $\eta$  is related to the ratio of the rotational to gravitational energy of the cloud core,  $\beta = E_{\text{rot}}/|E_g|$ , with  $\beta = 0.9\eta$ . Finally,  $\beta$  relates to the so-called “spin parameter,”  $\lambda = \sqrt{\beta}$ , that is most often used to characterize the angular momentum of dark matter halos (and their associated gas) formed from cosmological initial conditions (e.g., Barnes & Efstathiou 1987; Ryden 1988). The spin parameters of each cloud core are lognormally distributed with mean  $\lambda = 0.05$  and variance  $\sigma_\lambda^2 = 0.5$  (following Gardner 2001; O’Shea & Norman 2007).

Each model is run on a polar coordinate grid with  $512 \times 512$  spatial grid zones in  $r$  and  $\phi$ . The inner and outer boundary conditions allow for free outflow from the computational domain. Radial grid points are logarithmically distributed to allow for better numerical resolution toward the innermost region of the disk: the innermost cell outside of the sink region has a radius of approximately 0.1 AU and is 1.9 AU (both radially and azimuthally) at a radius of 100 AU.

Tan & McKee (2004) and Hosokawa et al. (2011) have shown that beyond 30–40  $M_\odot$  the role of increasing stellar luminosity becomes critically important to understanding the subsequent evolution of these protostars, as the intensely ionizing radiation begins to inhibit  $\text{H}_2$  formation, which is the primary coolant in the gas. We therefore terminate our simulations once the protostar reaches a mass of 40  $M_\odot$ .

#### 3.3 Evolution of the Protostellar Disk

Our fiducial model is characterized as a clump of gas roughly 0.5 pc in radius, with a mass of  $\sim 300 M_\odot$ , and at a temperature of 300 K. The spin parameter  $\lambda$  of the clump is equal to the mean of the distribution,  $\bar{\lambda} \simeq 0.05$ . The collapsing cores we model compare well to those derived from 3D numerical simulations inside primordial minihalos (Yoshida et al. 2006; Clark et al. 2011). Differences are attributable to our cores being toward the lower end of the mass spectrum that has been studied by these authors.

A quasi-Keplerian disk forms around the protostar within  $\sim 3$  kyr of the formation of the central protostar (in our fiducial model). The disk begins to fragment within a few hundred years after its formation. This timescale is somewhat longer than that found by Clark et al. (2011) and Greif et al. (2011), who used sink cells with smaller radii of 1.5 AU. However, this timescale is similar to that found by Smith et al. (2012a), who used sink cells with comparable radii of 20 AU (the central sink cell in our simulation being  $\sim 10$  AU in radius).

In Figure 1 we present three snapshots of the disk surface density inside of a 1000 AU radius and spanning 10 kyr of the disk evolution. The left panel shows that a rich density structure already

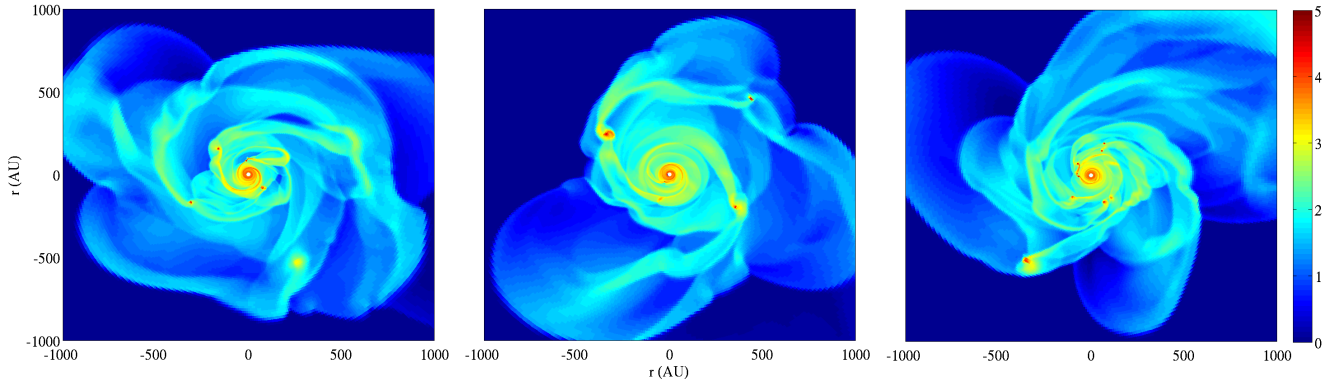


**Figure 1.** Projection of the disk surface mass density  $\Sigma$  within a  $2000 \times 2000$  AU volume centered on the accreting protostar. The time in each frame is  $t = 5, 10$ , and  $15$  kyr after formation of the protostar. **Left:** Some regions of the disk are Toomre-unstable, and several fragments can be identified at radii throughout the disk, between 10 and several hundred AU. **Center:** As these clumps are accreted onto the protostar or dispersed, the disk enters into a moderately quiescent period during which it is relatively stable against fragmentation. No fragments are present in the inner 300 AU of the disk. The three large fragments at radii beyond this are remnants from an earlier phase of fragmentation that had been raised to higher orbits. **Right:** Continued accretion from the parent cloud core builds up the mass of the disk, eventually triggering another period of vigorous fragmentation. The two fragments immediately to the left of the sink cell in this panel provide an example of how larger fragments can be sheared apart prior to being accreted through the sink cell, leading to intense and rapid variability in the accretion luminosity of the protostar.

exists within the disk a mere 5 kyr after formation of the central protostar. Together with the right panel, the clearly defined condensations of gas that have fragmented out of the disk indicate that the disk experiences multiple episodes of instability. The central panel presents an intermediary quiescent phase during which there is little to no fragmentation and the accretion of gas onto the protostar occurs relatively smoothly. The number of fragments within the disk clearly varies with time, as some fragments are tidally dispersed and others are accreted onto the central protostar; a result of the gravitational torques exerted by the fragments on each other and from larger spiral arm structures that form within the disk. Though accretion gradually drains the disk, new episodes of fragmentation are continually stimulated by the resupply of fresh gaseous material from the surrounding core envelope. It is also evident that most of the fragments are formed in the intermediate to outer disk region ( $\gtrsim 50$  AU), which is consistent with the numerical simulations of disks around protostars in the present-day universe (e.g., Stamatellos & Whitworth 2008; Clarke 2009).

Those fragments that pass through the inner computational boundary are assumed to be readily accreted by the central protostar. Though this boundary is not the protostellar surface itself, we can use the temperature (or more appropriately, the sound speed) of the disk material along this boundary to estimate the instantaneous mass accretion rate onto the protostar as

$$\dot{M} \approx \frac{c_s^3}{G} \quad (6)$$

(Shu 1977). In our fiducial model we find  $c_s$  is about  $2.0 \text{ km s}^{-1}$ . This corresponds to an instantaneous mass accretion rate of  $\sim 10^{-3} \text{ M}_\odot \text{ yr}^{-1}$ . We note that this is just below the critical (Eddington) accretion rate of  $\dot{M}_{\text{Edd}} \simeq 4.0 \times 10^{-3} \text{ M}_\odot \text{ yr}^{-1}$  above which the corresponding radiation pressure alone is capable of halting the accretion flow entirely (Hosokawa & Omukai 2009). This estimate matches the time averaged value of the mass accretion rate experienced by our model protostar (Figure 2), and is consistent with several other models of the runaway collapse of primordial gas as has been determined both analytically and from simulations (Omukai & Palla 2003; Bromm & Loeb 2004; Clark et al. 2011; Hosokawa et al. 2011; Smith et al. 2012b).

We present the complete mass accretion history for our fiducial model in the top panel of Figure 2. The formation of the protostar is marked by the sharp rise in the mass accretion rate, which we define as time  $t = 0$ . Following this, material from the surrounding envelope of the progenitor cloud core continues to stream onto the protostar at a rate of a few times  $10^{-3} \text{ M}_\odot \text{ yr}^{-1}$ . The mass of the protostar rapidly increases (within  $\sim 4$  kyr) to approximately  $15 \text{ M}_\odot$  before the accretion flow is temporarily halted by the formation of a quasi-Keplerian disk.

The disk modulates the subsequent accretion of disk material onto the protostar, with gravitational torques redistributing the mass and angular momentum of the infalling cloud core material. In VDB 2013 we demonstrated that the disk self-gravity quickly induces the formation of spiral arms. Furthermore, sections of the disk in which the local value of Toomre’s  $Q$  falls below unity become subject to fragmentation (Toomre 1964). These fragments are then torqued inward along ballistic trajectories before ultimately being accreted by the protostar, resulting in the episodic bursts of accretion (see Figure 2).

The cumulative effect of a quiescent mode of accretion that is punctuated by the episodic bursts is also evident in the curves of mass growth in the bottom panel of Figure 2. The protostellar mass (shown in blue) grows rapidly during the initial phase of smooth accretion (which lasts  $\sim 4$  kyr). However, the burst mode of accretion comes to dominate the subsequent growth of the protostar as is evident by the abrupt increases in the protostellar mass, typically a few  $\text{M}_\odot$  at a time. These increases are typically followed by plateaus during which the mass of the protostar changes very little as the disk equilibrates back into a quasi-Keplerian state. Each burst event is mirrored by a corresponding decrease in the total disk mass (in orange). However, the overall mass of the disk actually continues to increase in time due to the steady accretion of material from the remnant of the progenitor cloud core (the dashed black line in the top panel of Figure 2).

Additional details of the effects of the gravitational torques on the disk, and the resulting recurrent character of the disk fragmentation, are discussed in VDB 2013. Here we focus on the signature of this behavior on the protostellar accretion luminosity.

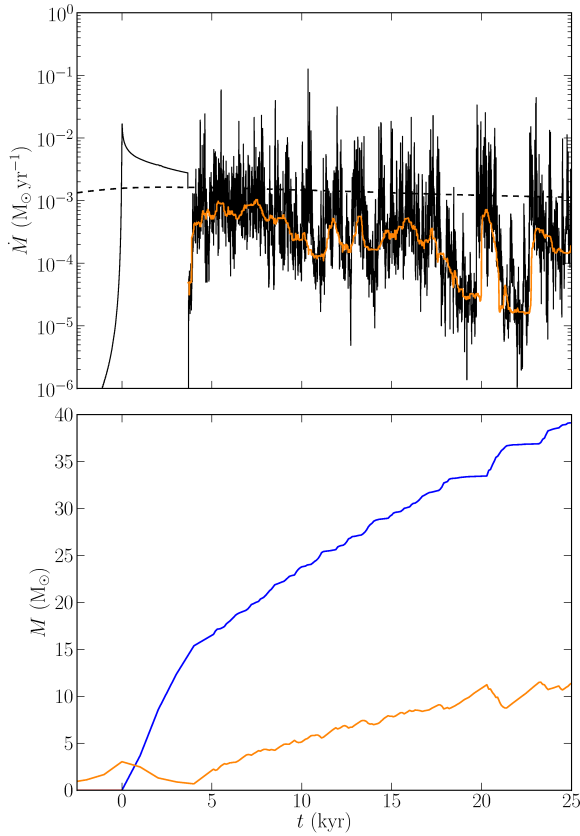


**Figure 2. Top:** Temporal evolution of mass accretion rates: from the cloud core onto the disk at 3000 AU (dashed black), and from the disk onto the protostar (solid black). The rectangular window time-averaged (in 1 kyr intervals) mass accretion rate—the quiescent accretion rate—is in orange. **Bottom:** Growth of the protostellar (blue) and disk (orange) masses in time. The protostellar mass grows via punctuated equilibrium, while the episodic increases in the mass of the protostar are coincident with the episodes of decline in disk mass. Nevertheless, the disk mass increases with time owing to the continually replenishment of disk material from the surround core material.

### 3.4 Accretion Luminosity

A protostar’s luminosity is a product of competition between mass growth from accretion and radiative loss from the protostellar interior. However, it is not until the protostar begins contracting toward the main sequence that its internally generated luminosity  $L_*$  surpasses the accretion luminosity  $L_{\text{acc}}$ . During the earliest stages of its evolution, the source of a protostar’s luminosity is almost entirely from accretion, so that  $L \approx L_{\text{acc}}$  (up to masses of  $M_* \approx 30\text{--}40 M_\odot$ ; Tan & McKee 2004; Hosokawa et al. 2011). In VDB 2013 we showed that the large variability in accretion experienced by the protostar results in accretion luminosities several orders of magnitude greater than might otherwise be expected (compare Clark et al. 2011, Hosokawa et al. 2011, and Smith et al. 2012b to VDB 2013, for example).

We estimate the accretion luminosity assuming that any material landing on the surface of the protostar has its kinetic energy dissipated radiatively at a rate

$$L = \frac{GM_* \dot{M}}{2R_*}, \quad (7)$$

where  $R_*$  is the protostellar radius.

In the absence of a detailed model for the stellar interior we instead fit the evolutionary models of Omukai & Palla (2003) with a piecewise power-law approximation to the radial expansion of the protostellar surface as a function of the protostar mass. Following formation of the hydrostatic core, the protostellar radius is expected to grow according to a mixed power-law as  $R_* \propto M_*^{0.27} \dot{M}_{-3}^{0.41}$ ; where  $\dot{M}_{-3}$  denotes the ratio of the actual instantaneous mass accretion rate  $\dot{M}$  to a value of  $10^{-3} M_\odot \text{ yr}^{-1}$  (Stahler et al. 1986; Omukai & Palla 2003). Increasing temperature within the core drives a luminosity wave outward, causing a rapid expansion of the stellar surface. When this wave breaches the protostellar surface, the interior is able to relax and the protostar begins Kelvin-Helmholtz contraction toward the main-sequence.

The following relations approximate the evolution of  $R_*$  through its transitions through these phases (Smith et al. 2012a):

$$R_* = \begin{cases} 26 M_*^{0.27} \dot{M}_{-3}^{0.41}, & M_* \leq M_1 \\ A_1 M_*^3, & M_1 < M_* < M_2 \\ A_2 M_*^{-2}, & M_* \geq M_2 \text{ and } R_* < R_{\text{MS}} \end{cases}. \quad (8)$$

The constants  $A_1$  and  $A_2$  are matching conditions that ensure the functional form of  $R_*$  is smoothly varying between transitions. The mass parameter  $M_1$  marks the transition between the adiabatic phase of growth and the arrival of the luminosity wave at the protostellar surface;  $M_2$ , the transition between the luminosity wave driven expansion and subsequent Kelvin-Helmholtz contraction.  $M_1$  and  $M_2$  are fixed by the instantaneous mass accretion rate as the protostar transitions between phases, and are defined as

$$\begin{aligned} M_1 &= 5 \dot{M}_{-3}^{0.27}, \\ M_2 &= 7 \dot{M}_{-3}^{0.27}. \end{aligned} \quad (9)$$

Note that as the evolution of the protostellar interior occurs roughly adiabatically, due to the long cooling time therein, the variability in the accretion rate induced by the burst mode of accretion does not result in significant variability in the radius of the protostar.

The accretion luminosity calculated for our fiducial model is shown in Figure 3 (black). In overlay is the time averaged rate (i.e., the quiescent rate,  $L_q$ , in orange), and a demarcation  $10\times$  greater than the quiescent rate (dashed orange). Accretion events during which  $L$  exceeds  $L_q$  by the factor of 10 are highlighted (dashed blue). Once the protostar is formed (designated as  $t = 0$ ),  $L$  climbs very quickly to  $\sim 10^4 L_\odot$ . The luminosity remains at about this level during the period of smooth accretion until a disk is formed at  $t \sim 4$  kyr. Although the mean rate remains at roughly  $10^4 L_\odot$ , the episodic nature of the subsequent vigorous accretion gives rise to significant variability, with some peaks reaching several times  $10^6 L_\odot$ —two orders of magnitude greater than  $L_q$ . One might expect this large variability in luminosity caused by the individual burst events to affect the accretion flow via feedback from the enhanced radiation field. However, as the duration of the individual bursts are quite short (typically on the order of a few times 100 yr), we expect that they do not have any appreciable effect on the long-term growth of the protostar.

In the bottom panel of Figure 3 we focus on a 1 kyr window of our simulation in order to highlight our burst identification scheme. We calculate the effective mean accretion rate (the solid orange line) using a moving 1 kyr window. As burst events are ultimately attributable to the accretion of large individual fragments (with masses on the order of  $0.1\text{--}1 M_\odot$ ) and have an overall mean duration of a few times 100 yr, the use of a 1 kyr moving window allows us to suppress variations due to the large fragments being sheared apart into several smaller ones, each of which is accreted



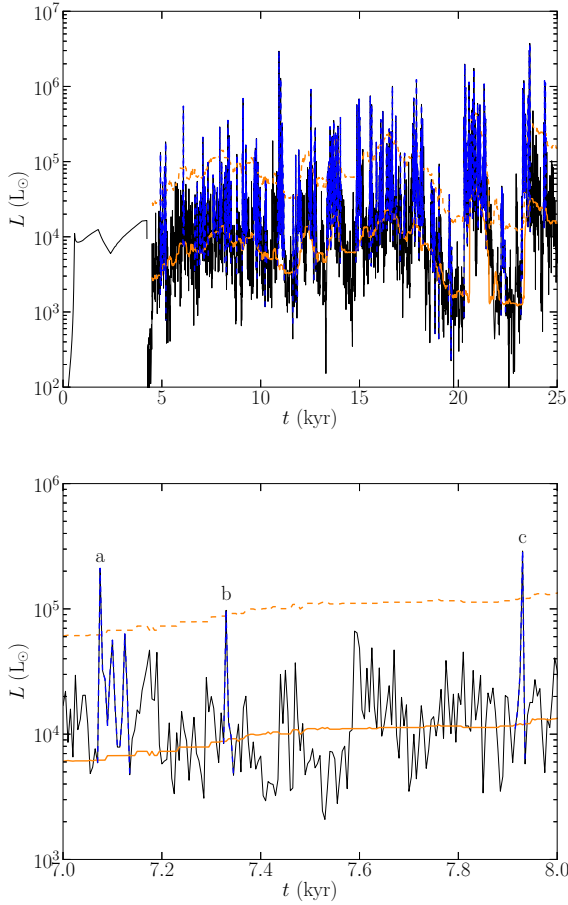


**Figure 3. Top:** Temporal evolution of the (accretion) luminosity from the protostar in our fiducial model (in black). In overlay is the time averaged quiescent rate (solid orange), and the  $10 \times L_q$  rate (dashed orange), with those accretion events whose peak luminosity exceeds this threshold highlighted in blue. **Bottom:** A zoom in on a 1 kyr window of the luminosity history for clarity. Accretion events in excess of  $10 \times L_q$  are clearly identified (labeled, a, b, and c, and highlighted in blue).

by the protostar in rapid succession (VDB 2013). Hence, we also include as part of a single burst event all points left- and rightward of the peak luminosity that are greater than the mean (and not only those points for which  $L$  is strictly  $> 10 \times L_q$ ).

#### 4 CLUSTERS OF POPULATION III PROTOSTARS

Figure 4 illustrates how the burst mode in individual protostars can sum to produce a cluster luminosity. For simplicity, we consider a cluster of only two stars, with one being our fiducial model with  $\lambda = 0.05$ , and the second characterized by  $\lambda = 0.065$  but forming 5 kyr after the first. The panels in the top- and middle-left column are the luminosities of the individual cluster members while the bottom-left shows the cumulative luminosity for the cluster as a whole. The histograms on the right-hand side present statistics of the fractional number distribution of burst events  $f_b$  of different duration  $\Delta t_b$ . These can be used as metrics to evaluate differences between the individual and cluster luminosities.

Prior to  $t = 5$  kyr, before the second cluster member forms, the luminosity of the cluster is of course just the luminosity of the

first and as yet sole member. The second cluster member begins its evolution from  $t \sim 5$  kyr (where time  $t = 0$  marks the formation of the first cluster member). In the subsequent  $\sim 2$  kyr, as the second cluster member smoothly accretes material from its surroundings, its contribution to the total cluster luminosity increases. In fact, comparing the cluster luminosity to the individual component luminosities reveals that a significant amount of the variability in the luminosity of the first cluster member is being completely obscured. During this time, the cluster luminosity is consistently above  $\sim 10^4 L_{\odot}$ . By  $t \sim 7$  kyr, both cluster members harbor their own protostellar disks, and accretion onto each protostar is being driven by the action of gravitational torques in the massive disks surrounding each host—i.e., via the burst mode of accretion. Correspondingly, the cluster luminosity thereafter exhibits a significant amount of variability, comparable to that of either of its component members.

In the right-hand column of Figure 4 we present histograms of the duration of the burst events exhibited by the individual cluster members (top- and middle-right), and for the cluster as a whole (bottom-right). The first cluster member exhibits a total of 73 individual burst events over the course of  $\sim 20.5$  kyr—the span of time from when the disk forms to when the protostar reaches a mass of  $\sim 40 M_{\odot}$  and the simulation is terminated. The mean burst duration is found to be  $\sim 96.3$  yr. This amounts to approximately 7.0 kyr that are spent exclusively in the burst mode of accretion, with the remaining 13.5 kyr spent in quiescent phases. By comparison, during the approximately 18.5 kyr from the time the second cluster member forms to when the simulations end, the second cluster member exhibits a total of 68 individual burst events. The typical burst duration is found to be  $\sim 80.2$  yr, for a total of  $\sim 5.5$  kyr spent accreting via the burst mode, and the remaining roughly 13.0 kyr spent in quiescent phases.

From this we can conclude that the burst mode of accretion plays a significant role in the mass growth of Population III protostars. In both cases about 30% of each protostar’s individual accretion history is spent in the burst mode—that is to say that gravitational-instability-driven fragmentary accretion is responsible for one-third to one-half of the total accretion onto the first stars. This is actually a significantly higher proportion of time than has been observed in analogous simulations of present-day star formation, wherein the burst mode of accretion is thought to be responsible for only  $\sim 10\%$  of a protostar’s accretion history (e.g., Vorobyov & Basu 2006, 2010; VDB 2013).

The number and frequency of the observed bursts is also affected by whether one considers each cluster member individually or simply considers the cumulative luminosity of the cluster as a whole. The first and second cluster member yield 73 and 68 burst events over 18.5 and 13.0 kyr, respectively—1 event roughly every 200 yr in both cases. Performing the same analysis of the luminosity, but of the cluster as a whole, the perceived number of burst events would be only 74: far fewer than might be expected given the number of actual burst events experienced by the cluster’s component members.

Hence, the quiescent mode is clearly the dominant mode of accretion. As it is unlikely for all members of a cluster to be dimming simultaneously, the variations below the quiescent rate in the luminosity of a single cluster member rate are largely obscured. The cluster luminosity is thus somewhat greater than might be suggested by a simple summation of the individual luminosities. Hence, the number of burst events as determined by examining the cluster luminosity is actually fewer than might be expected, because individual burst events can only be identified when the lu-

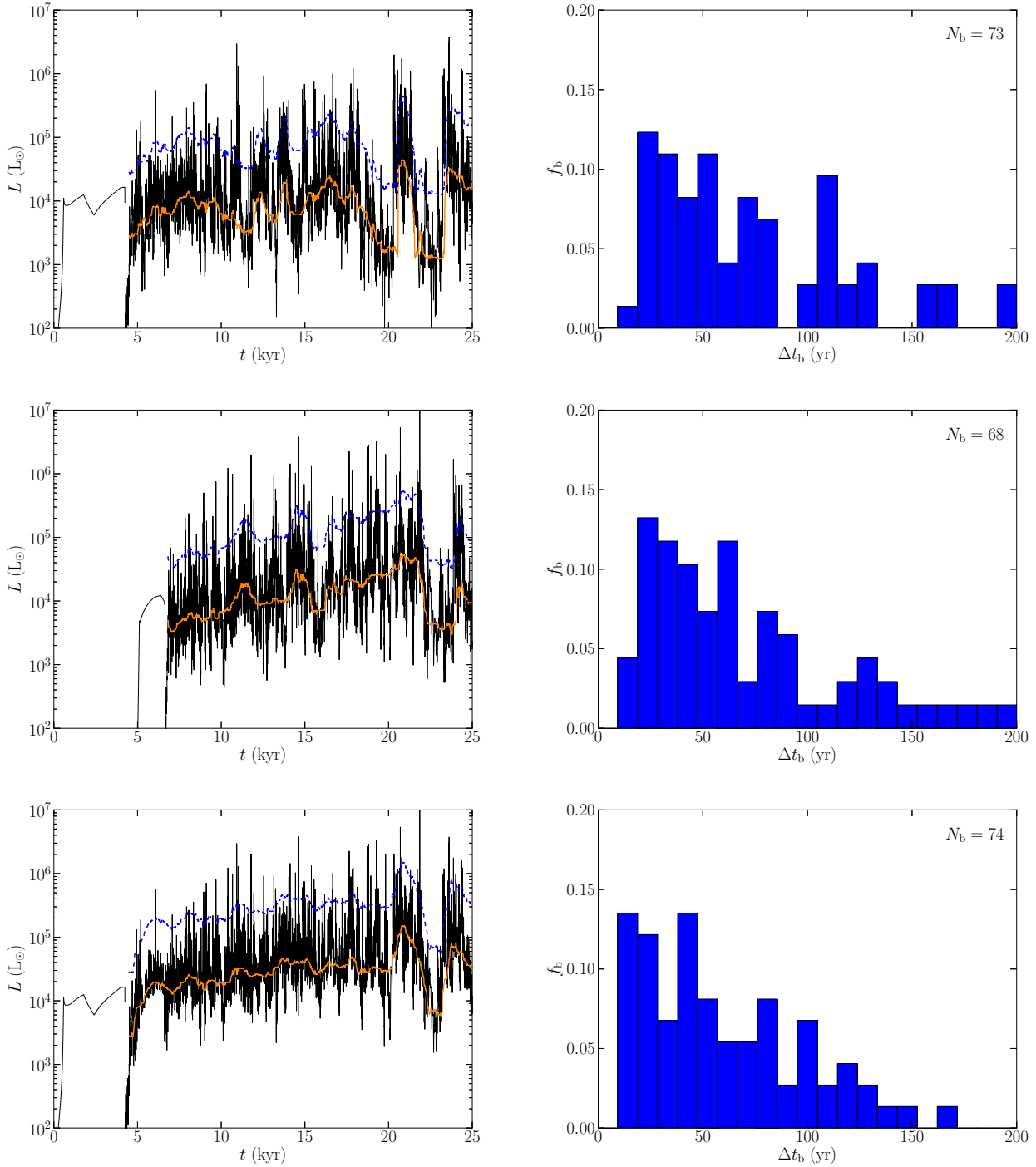


**Figure 4.** Accretion luminosity  $L$  and distribution of burst durations of the individual cluster members (top and middle panels) and for their combined output (bottom panel) in our example  $N = 2$  member cluster. The top panel is our fiducial model with  $\lambda = 0.050$ ; the middle panel is a model with  $\lambda = 0.065$ . **Left:** Accretion luminosities  $L$  are in black; the quiescent luminosity  $L_q$  is in orange; the dashed blue line indicates a luminosity  $10 \times L_q$ . Note that the top panel is the fiducial model also shown in Figure 3. **Right:** Fractional number distributions ( $f_b$ ) of burst durations ( $\Delta t_b$ ) for the individual cluster members (top and middle), and for the cumulative cluster profile (bottom). The total number of identified bursts ( $N_b$ ) is indicated in the upper-right of each panel. The approximate mean burst duration observed for the individual cluster members are 96.3 and 80.2 yr, respectively. The mean burst duration for the cumulative cluster luminosity profile is  $\sim 72.0$  yr.

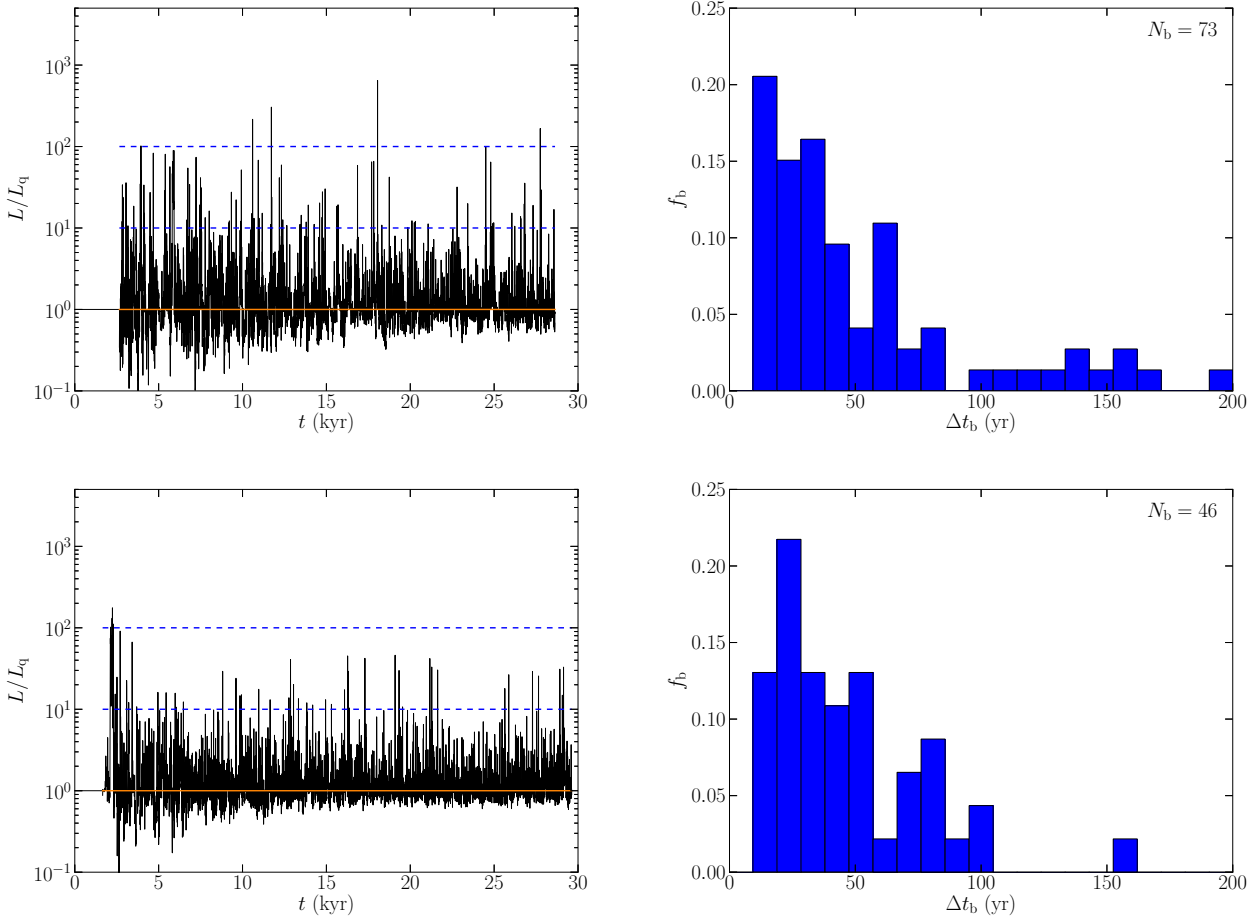


**Figure 5.** Normalized accretion luminosities  $L/L_q$  (left column) and histograms of the fractional number distributions of burst durations (right column) for two additional clusters containing  $N = 16$  (top), and  $N = 128$  (bottom) members. The dashed blue lines in the left panels denote thresholds of 10 and  $100\times$  the quiescent luminosity; all other lines and colors are as they appear in Figure 4. The normalized quiescent luminosity in each case corresponds to approximately  $4 \times 10^5$  and  $4 \times 10^6 L_\odot$ , respectively. During the evolution of the  $N = 16$  cluster a confluence of burst events at  $t \approx 18$  kyr produce a particularly prominent luminous event that is  $647\times$  more luminous than the cluster’s quiescent level. However, the competition between the increasing cluster quiescent luminosity  $L_q$  and the potential for such overlapping bursts is evident in the reduced magnitude of the fluctuations above  $L_q$  with increasing cluster size  $N$ . In the right panels, the total number of identified bursts ( $N_b$ ) is indicated in the upper-right.

minosity of an individual star exceeds the luminosity of the cluster as a whole. As a result, the perceived duration of burst events also decreases.

To compare the variations in the luminosities of clusters of different size  $N$ , we normalize each cluster luminosity  $L$  by its own quiescent rate  $L_q$ , and in Figure 5 compare them for clusters with  $N = 16$  and  $N = 128$ . Luminosities are plotted in black; quiescent cluster luminosities in orange; and the dashed blue lines denote luminosity levels  $10\times$  and  $100\times$  the quiescent rate  $L_q$ . The panels show that for larger  $N$  it is less likely that there are burst events for which the cluster luminosity reaches above a certain multiple of  $L_q$ . Conversely, as  $N$  increases, there is also the possibility that two or more cluster members will experience simultaneous independent burst events. We use Figure 6 to illustrate how the time-averaged quiescent luminosity  $\langle L_q \rangle$  increases with the number  $N$  of cluster members. The best-fit line represents a linear relationship. For completeness, we model clusters as large as  $N = 1000$ , however most estimates of Population III clustering would imply much smaller clusters, as discussed earlier in this paper.

In Figure 7, the vertical axis shows the duration of time  $\Delta t$

as a fraction of the cluster’s total star-forming lifetime  $t$  that a cluster spends above a certain luminosity threshold. The horizontal axis shows the sizes  $N \in \{2, 4, 8, 16, 32, 64, 128, 256, 1024\}$  of the individual primordial star-forming clusters. Each curve represents a specific luminosity threshold: from top to bottom, of 5, 10, 20, 50, and 100 times each specific cluster’s quiescent luminosity. The diamond symbols along a single value of  $N$  thus indicate how much time that cluster spends at an elevated luminosity  $L/L_q$ . As the typical time frame for an individual burst event is on the order of a few hundred yr, the likelihood of two or more protostars within a cluster expressing simultaneous burst events is quite low. As the number of cluster members increases however, such coincidences become increasingly likely. However, this effect is counteracted by the fact that each additional protostar in a cluster also contributes to increasing the mean cluster luminosity. This prohibits all but the most intense burst accretion events from being visible. A balance between these effects is achieved for relatively small clusters,  $N \simeq 16$ . For these cases, we find nearly 15% of the cluster’s star forming period is spent at a luminosity level  $10\times$



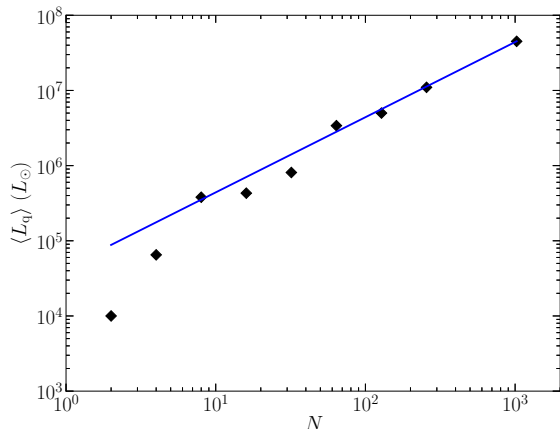


**Figure 6.** The time-averaged quiescent luminosity  $\langle L_q \rangle$  in clusters of size  $N \in \{2, 4, 8, 16, 32, 64, 128, 256, 1024\}$  (from left to right) represented by diamond symbols.  $\langle L_q \rangle$  increases roughly linearly as a function of the number  $N$  of cluster members as shown by the best fit line.

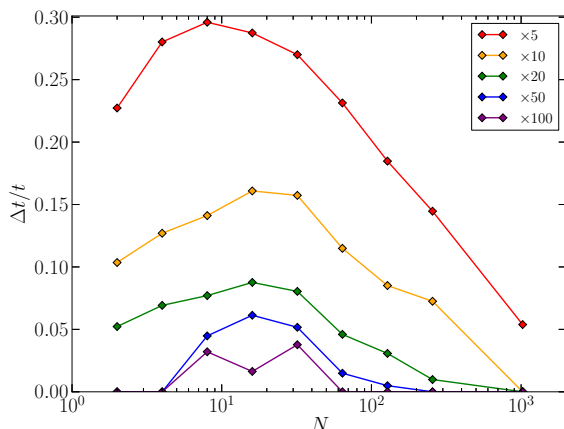


**Figure 7.** The fractional duration of total time,  $\Delta t/t$ , that a cluster of a given size  $N$  spends at an elevated luminosity. Shown are the values of  $\Delta t/t$  for different values of elevated luminosity  $L/L_q = 5, 10, 20, 50$ , and  $100$  (appearing sequentially top to bottom). Most curves show a maximum at  $N \approx 16$ . Larger clusters exhibit decreasing variability above the mean quiescent rate  $\langle L_q \rangle$ .

greater than the mean rate,  $L_q$ . This corresponds to an absolute luminosity approaching  $10^8 L_\odot$ .

## 5 DISCUSSION & CONCLUSIONS

We have presented a scenario for the assembly of a cluster of first stars formed from the pristine gas that is pooling into newly virialized dark matter halos at redshift  $z \sim 20\text{--}50$ . The Jeans criterion provides a context for the combination of self-gravity and anisotropic structure to give rise to fragmentation of the gas. We estimate that a typical dark matter halo with mass between  $10^5$  and  $10^6 M_\odot$  contains 10% by mass of gas, of which roughly 10% actually goes into stars. The Jeans criterion then implies the formation of clusters containing tens of members (perhaps 10–50 protostars), though the specific numbers are difficult to estimate due to the am-

biguity with which the dispersal and merger of clumps prior to their collapse occurs (e.g., Greif et al. 2011).

We employ numerical hydrodynamics simulations in the thin-disk limit to then investigate the long-term evolution of the individual clumps. We model their collapse self-consistently into the formation of the protostar and its surrounding disk. In each case a disk forms relatively quickly, regardless of the initial conditions, within a few kyr of the formation of the protostar. The disk is centrifugally supported, but its mass lends it to being gravitationally unstable. We observe a rapid and episodic fragmentation of the disk during which fragments having between  $0.1\text{--}1.0 M_\odot$  are formed at typical radii of  $\sim 50$  AU. The fragments are torqued inward toward the central protostar where they are then accreted, resulting in massive bursts of luminosity that can exceed the mean rate by as much as two orders of magnitude, occasionally exceeding  $10^6 L_\odot$  (as in Figure 4).

In the context of this formation scenario we analyze the luminosity profiles that are produced by a multiplicity of first stars having formed approximately coevally within a young cluster. We assume that each cluster member forms independently and harbors its own disk that is subject to gravitationally induced episodic fragmentation and accretion (i.e., the burst mode of accretion). With increasing numbers of cluster members, the quiescent luminosity of the cluster is seen to steadily increase. However, increases in the number of cluster members also increase the probability that two or more members experience a burst of accretion simultaneously. In one cluster simulation we observe one such particularly luminous super-posed accretion event during which the cluster luminosity rises to nearly  $1000\times$  its quiescent rate, to  $2.48 \times 10^8 L_\odot$  (Figure 5).

Competition between these two effects results in clusters of a certain size ( $N \approx 16$ ) spending a sizable fraction of their star forming life-time (roughly 15%) at luminosities  $10\times$  greater than might otherwise be expected with smooth accretion (e.g., Smith et al. 2012a). Each additional object added to a cluster raises the mean/quiescent luminosity of the cluster, and this in turn tends to suppress the prominence of individual and multiple burst events in clusters in which  $N \gtrsim 16$ . Such moderately sized clusters are also the most easily manufactured, capable of being produced assuming even a relatively low star formation efficiency, and are of a number as has been counted in a variety of theoretical Population III star forming scenarios to date (e.g., Stacy et al. 2010; Clark et al. 2011; Greif et al. 2011).

The possible formation of clusters of Population III stars in the dark matter halos of the early universe provides a unique opportunity for observations. Rydberg et al. (2013) estimated the total luminosity from even the most upper mass estimates of Population III stars (i.e., those with masses  $\sim 300 M_\odot$ ) and found that even these were likely too faint to be observed by next-generation telescopes such as the James Webb Space Telescope. The likelihood for such instruments to observe even lower mass Population III stars is thus highly improbable. However, as we have shown, clusters of even low mass Population III stars (as others have also indicated may exist: Bromm et al. 2003; Clark et al. 2008; and Greif et al. 2012), are capable of producing luminosities in excess of lone very massive Population III stars (for example Bromm et al. (2001) estimate luminosities in the range  $\approx 10^6\text{--}10^7 L_\odot$  for masses in the range  $100\text{--}500 M_\odot$ ). Observational constraints on the early stages of reionization, from 21 cm observations by the Square Kilometer Array (e.g., Carilli et al. 2004) may actually provide indirect constraints on the abundance of such clusters. Observations by the Atacama Large Millimeter/submillimeter Array (ALMA) of emission

from dusty galaxies in the early universe may also provide insight into their possible formation as influenced by the formation of an initial cluster of Population III stars. However, it will be in the next decade that next-generation telescopes may actually provide direct constraints on the Population III star formation taking place in the early universe; with clusters of Population III stars being some of the most luminous at that epoch.

## ACKNOWLEDGEMENTS

We thank Eduard Vorobyov for early discussions and the anonymous referee for comments that improved the presentation of the paper. SB acknowledges support from a Discovery Grant from the Natural Sciences and Engineering Research Council (NSERC) of Canada. This research has made use of NASA's Astrophysics Data System.

## REFERENCES

- Abel T., Anninos P., Norman M. L., Zhang Y., 1998, *ApJ*, 508, 518
- Abel T., Bryan G. L., Norman M. L., 2002, *Science*, 295, 93
- Barnes J., Efstathiou G., 1987, *ApJ*, 319, 575
- Basu S., 1997, *ApJ*, 485, 240
- Basu S., Ciolek G. E., Wurster J., 2009, *New. Astron.*, 14, 221
- Bond J. R., Arnett W. D., Carr B. J., 1984, *ApJ*, 280, 825
- Bromm V., Coppi P. S., Larson R. B., 1999, *ApJL*, 527, L5
- Bromm V., Coppi P. S., Larson R. B., 2002, *ApJ*, 564, 23
- Bromm V., Kudritzki R. P., Loeb A., 2001, *ApJ*, 552, 464
- Bromm V., Loeb A., 2004, *Nature*, 9, 353
- Carpenter J. M., Meyer M. R., Dougados C., Strom S. E., Hillenbrand L. A., 1997, *AJ*, 114, 198
- Ciardi B., Ferrara A., 2001, *MNRAS*, 324, 648
- Ciolek G. E., Basu S., 2006, *ApJ*, 652, 442
- Clark P. C., Glover S. C. O., Klessen R. S., 2008, *ApJ*, 672, 757
- Clark P. C., Glover S. C. O., Smith R. J., Greif T. H., Klessen R. S., Bromm V., 2011, *Science*, 331, 1040
- Clarke C. J., 2009, *MNRAS*, 396, 1066
- Clarke C. J., Bromm V., 2003, *MNRAS*, 343, 1224
- Commerçon B., Hennebelle P., Audit E., Chabrier G., Teyssier R., 2010, *A&A*, 510, L3
- Dapp W. B., Basu S., 2009, *MNRAS*, 395, 1092
- Dapp W. B., Basu S., Kunz M. W., 2012, *A&A*, 541, A35
- Ferrara A., Pettini M., Shchekinov Y., 2000, *MNRAS*, 319, 539
- Gardner J. P., 2001, *ApJ*, 557, 616
- Gnedin N. Y., Ostriker J. P., 1997, *ApJ*, 486, 581
- Greif T. H., Bromm V., Clark P. C., Glover S. C. O., Smith R. J., Klessen R. S., Yoshida N., Springel V., 2012, *MNRAS*, 424, 399
- Greif T. H., Springel V., White S. D. M., Glover S. C. O., Clark P. C., Smith R. J., Klessen R. S., Bromm V., 2011, *ApJ*, 737, 75
- Gutermuth R. A., Megeath S. T., Myers P. C., Allen L. E., Pipher J. L., Fazio G. G., 2009, *ApJS*, 184, 18
- Heitsch F., Hartmann L. W., Burkert A., 2008, *ApJ*, 683, 786
- Heitsch F., Slyz A. D., Devriendt J. E. G., Hartmann L. W., Burkert A., 2006, *ApJ*, 648, 1052
- Hillenbrand L. A., 1997, *AJ*, 113, 1733
- Hirano S., Hosokawa T., Yoshida N., Umeda H., Omukai K., Chiaki G., Yorke H. W., 2014, *ApJ*, 781, 60
- Hosokawa T., Omukai K., 2009, *ApJ*, 691, 823
- Hosokawa T., Omukai K., Yoshida N., Yorke H. W., 2011, *Science*, 334, 1250
- Johnson J. L., 2010, *MNRAS*, 404, 1425
- Johnstone D., Wilson C. D., Moriarty-Schieven G., Joncas G., Smith G., Gregersen E., Fich M., 2000, *ApJ*, 545, 327
- Lada C. J., Lada E. A., 2003, *ARA&A*, 41, 57
- Lin C. C., Mestel L., Shu F. H., 1965, *ApJ*, 142, 1431
- Machida M. N., Inutsuka S.-i., Matsumoto T., 2011, *ApJ*, 729, 42
- Mellon R. R., Li Z.-Y., 2008, *ApJ*, 681, 1356
- Miralda-Escudé J., Rees M. J., 1997, *ApJL*, 478, L57
- Omukai K., Nishi R., 1998, *ApJ*, 508, 141
- Omukai K., Palla F., 2003, *ApJ*, 589, 677
- Omukai K., Tsuribe T., Schneider R., Ferrara A., 2005, *ApJ*, 626, 627
- Onishi T., Mizuno A., Kawamura A., Ogawa H., Fukui Y., 1998, *ApJ*, 502, 296
- O'Shea B. W., Norman M. L., 2007, *ApJ*, 654, 66
- Price D. J., Bate M. R., 2008, *MNRAS*, 385, 1820
- Rydberg C.-E., Zackrisson E., Lundqvist P., Scott P., 2013, *MNRAS*, 429, 3658
- Ryden B. S., 1988, *ApJ*, 329, 589
- Safranek-Shrader C., Milosavljević M., Bromm V., 2014, *MNRAS*, 438, 1669
- Scannapieco E., Schneider R., Ferrara A., 2003, *ApJ*, 589, 35
- Shu F. H., 1977, *ApJ*, 214, 488
- Smith R. J., Hosokawa T., Omukai K., Glover S. C. O., Klessen R. S., 2012a, *MNRAS*, p. 3212
- Smith R. J., Hosokawa T., Omukai K., Glover S. C. O., Klessen R. S., 2012b, *MNRAS*, 424, 457
- Stacy A., Greif T. H., Bromm V., 2010, *MNRAS*, 403, 45
- Stacy A., Greif T. H., Bromm V., 2012, *MNRAS*, 422, 290
- Stahler S. W., Palla F., Salpeter E. E., 1986, *ApJ*, 302, 590
- Stamatellos D., Whitworth A. P., 2008, *A&A*, 480, 879
- Stone J. M., Norman M. L., 1992, *ApJS*, 80, 753
- Tan J. C., McKee C. F., 2004, *ApJ*, 603, 383
- Tegmark M., Silk J., Rees M. J., Blanchard A., Abel T., Palla F., 1997, *ApJ*, 474, 1
- Tomida K., Okuzumi S., Machida M. N., 2015, *ArXiv e-prints*
- Toomre A., 1964, *ApJ*, 139, 1217
- Tornatore L., Ferrara A., Schneider R., 2007, *MNRAS*, 382, 945
- Tumlinson J., Shull J. M., 2000, *ApJL*, 528, L65
- Turk M. J., Abel T., O'Shea B., 2009, *Science*, 325, 601
- Turk M. J., Oishi J. S., Abel T., Bryan G. L., 2012, *ApJ*, 745, 154
- Vorobyov E. I., Basu S., 2005, *ApJL*, 633, L137
- Vorobyov E. I., Basu S., 2006, *ApJ*, 650, 956
- Vorobyov E. I., Basu S., 2010, *ApJ*, 719, 1896
- Vorobyov E. I., DeSouza A. L., Basu S., 2013, *ApJ*, 768, 131
- Windhorst R. A., Cohen S. H., Jansen R. A., Conselice C., Yan H., 2006, *New Astron. Rev.*, 50, 113
- Yoshida N., Abel T., Hernquist L., Sugiyama N., 2003, *ApJ*, 592, 645
- Yoshida N., Omukai K., Hernquist L., 2008, *Science*, 321, 669
- Yoshida N., Omukai K., Hernquist L., Abel T., 2006, *ApJ*, 652, 6